

Ion Channel Biosensors—Part II: Dynamic Modeling, Analysis, and Statistical Signal Processing

Vikram Krishnamurthy, *Fellow, IEEE*, Sahar Moradi Monfared, and Bruce Cornell

Abstract—This paper deals with the dynamic modeling, analysis, and statistical signal processing of the ion channel switch biosensor. The electrical dynamics are described by a second-order linear system. The chemical kinetics of the biosensor response to analyte concentration in the reaction-rate-limited regime are modeled by a two-timescale nonlinear system of differential equations. Also, the analyte concentration in the mass-transport-influenced regime is modeled by a partial differential equation subject to a mixture of Neumann and Dirichlet boundary conditions. By using the theory of singular perturbation, we analyze the model so as to predict the performance of the biosensor in transient and steady-state regimes. Finally, we outline the use of statistical signal processing algorithms that exploit the biosensor dynamics to classify analyte concentration.

Index Terms—

I. INTRODUCTION

THE COMPANION paper (Part I) described the construction and experimental studies of the *ion channel switch* (ICS) biosensor. The ICS biosensor provides an interesting example of engineering at the nanoscale [1]. Its functionality depends on approximately 100 lipids and a single ion channel modulating the flow of billions of ions in a typical sensing event of approximately 5 min. Our modeling and analysis in this paper will capture these salient features. Because the biosensor can detect analyte concentrations smaller than 1 picomolar, mass transfer of analyte over the electrodes becomes the dominant design criterion. This requires careful modeling of the chemical kinetics (how the analyte molecules interact with the binding sites), together with the mass transport dynamics of fluid flow (how analyte molecules flow onto the electrodes). Finally, the intrinsically digital output from the biosensor permits the use of sophisticated statistical signal processing algorithms to estimate the type and concentration of analyte.

A. Main Results

The following are our main results.

1) *Modeling of Biosensor Electrical Response and Chemical Kinetics*: In Section II, we give a complete model description

of the electrical response and chemical kinetics of the biosensor. The electrical dynamics of the ICS biosensor are described by an equivalent second-order linear system. The chemical kinetics detail how the biosensor responds to analyte molecules—from analyte molecules binding to the receptors to the eventual disruption of the ability of gramicidin molecules to form dimers. Thus, we convert the qualitative description of the biosensor operation given in the companion paper into mathematical equations for a dynamical system.

2) *Analyte Flow and Analysis of Biosensor Dynamics*: In Section III, we analyze the biosensor dynamics. We show via eigen decomposition that the biosensor response to analyte concentration has a two-timescale behavior. This permits analysis of the chemical kinetics as a *singularly perturbed* system [2], [3]. One of the highlights of this analysis is that it mathematically justifies the experimentally observed response of the biosensor to analyte concentration. Another highlight of our modeling and analysis is that we can predict the biosensor performance at very low analyte concentrations (e.g., picomolar to femtomolar). In such cases, it is necessary to consider the analyte flow and its interaction with the receptors at the biosensor electrode. We model the analyte flow as a diffusion-type partial differential equation, which interacts with the chemical kinetics when analyte molecules interact with the biosensor. This results in Neumann and Dirichlet boundary conditions [4]–[6]. We show that this model accurately predicts the biosensor performance at low analyte concentrations.

3) *Statistical Signal Processing*: A further goal of detailed modeling and analysis of the biosensor is to design sophisticated statistical signal processing algorithms that exploit these model dynamics to classify analytes and estimate their concentrations. In Section IV, we illustrate how statistical signal processing algorithms can be used to detect the presence of analyte.

B. Related Work

The companion paper provided a literature review of biosensors involving ion channels and tethered lipid membranes. Here, we outline related work in modeling, analysis, and statistical signal processing involving biosensors. The equivalent electrical model we introduce in Section II-A for the lipid membrane, interfacial capacitance, and electrolyte resistance is similar to that used in electrophysiological models of cell membranes, see [7] for a textbook treatment. The conceptual idea behind electrophysiological models originates from the work of Cole, who pioneered the notion that cell membranes could be likened to an electronic circuit [8]. The chemical kinetics discussed in Section II-B result in a system of nonlinear ordinary differential equations. The work of Lauffenburger and

Manuscript received May 11, 2009; revised August 20, 2009 and January 6, 2010. First published; current version published. The review of this paper was arranged by Associate Editor xxx.

V. Krishnamurthy and S. M. Monfared are with the Department of Electrical and Computer Engineering, University of British Columbia, Vancouver, BC V6T 1Z4, Canada (e-mail: vikramk@ece.ubc.ca; smonfare@ece.ubc.ca).

B. Cornell is with Surgical Diagnostics Ltd., St Leonards, N.S.W. 2065, Australia (e-mail: brucec@surgicaldiagnostics.com).

Color versions of one or more of the figures in this paper are available online at <http://ieeexplore.ieee.org>.

Digital Object Identifier 10.1109/TNANO.2010.2041466

87 Linderman [9] is an excellent example of such chemical kinetics
 88 ics and binding. Similar models have been adopted in a lateral
 89 flow bioreactor in [10]. The singular perturbation methods
 90 we use in Section III-A are well known in nonlinear systems
 91 theory, see [2]. More sophisticated stochastic singular pertur-
 92 bation methods are studied in [11]. The mass transport dy-
 93 namics (partial differential equation) coupled with chemical
 94 kinetics discussed in Section III-B results in a diffusion partial
 95 differential equation with Neumann and Dirichlet boundary
 96 conditions [4]–[6]. Similar formulations for binding and dis-
 97 sociation between a soluble analyte and an immobilized lig-
 98 and are studied in [12]. Mass transport dynamics are formu-
 99 lated in [4] and [13] for a two-compartment model where ana-
 100 lyte molecules move between the two compartments. Goldstein
 101 *et al.* [6] discuss the accuracy and theoretical basis of different
 102 models for mass transport effects in the binding of analytes.
 103 Dehghan [14] discusses several different finite-difference meth-
 104 ods to solve the advection–diffusion equation and the stability of
 105 the numerical methods. Finally, the statistical signal processing
 106 of ion channel currents (Section IV) is an active area of research
 107 with several papers published since the 1990s. Hidden Markov
 108 models (HMMs) have been widely used, see [15] and [16] and
 109 references therein.

110 II. MODELING THE DYNAMICS OF THE ICS BIOSENSOR

111 This section constructs mathematical models for the ICS
 112 biosensor’s response to analyte molecules. In Section II-A and
 113 II-B, white-box models for the electrical response and chemi-
 114 cal kinetics are formulated. Finally, a black-box model for the
 115 biosensor response based on experimental observations is given
 116 in Section II-C. This sets the stage for Section III where the
 117 white-box models are analyzed, resulting in a mathematical jus-
 118 tification of the black-box model.

119 A. Electrical Dynamics of the Biosensor

120 The ICS biosensor can be viewed as a biological transistor.
 121 Fig. 1(a) illustrates the equivalent circuit of the biosensor
 122 before and after the detection of analyte. Fig. 1(b) details the
 123 components of the equivalent circuit. The resistor $1/G$ models the
 124 biosensor resistance and increases with the presence of analyte.
 125 C_1 denotes the capacitance of the membrane, while C_2 denotes
 126 the interfacial capacitance of the gold substrate. Note that one
 127 face of the capacitor C_2 is charged due to ions in solution,
 128 the other face is due to electrons that form the output current
 129 of the biosensor. Thus, C_2 provides the interface between the
 130 biological sensor (which, as with biological systems, operates
 131 on ion flow) and the electron flow of electrical instrumentation.
 132 R_2 denotes the resistance of the electrolyte, and its value varies
 133 depending on the type of electrolyte and the dimensions of the
 134 return path in the bathing sample solution. In a flow chamber,
 135 the dimensions of the return path can be sufficiently small so that
 136 R_2 becomes significant. The values of C_1 , C_2 , R_1 , and R_2
 137 are functions of electrode area. Typical values for 2009 generation
 138 of ICS biosensors are listed in Table I.

139 Let V_{out} denote the external applied potential and i denote
 140 the output current as depicted in Fig. 1(b). With $V_{\text{out}}(s)$ and

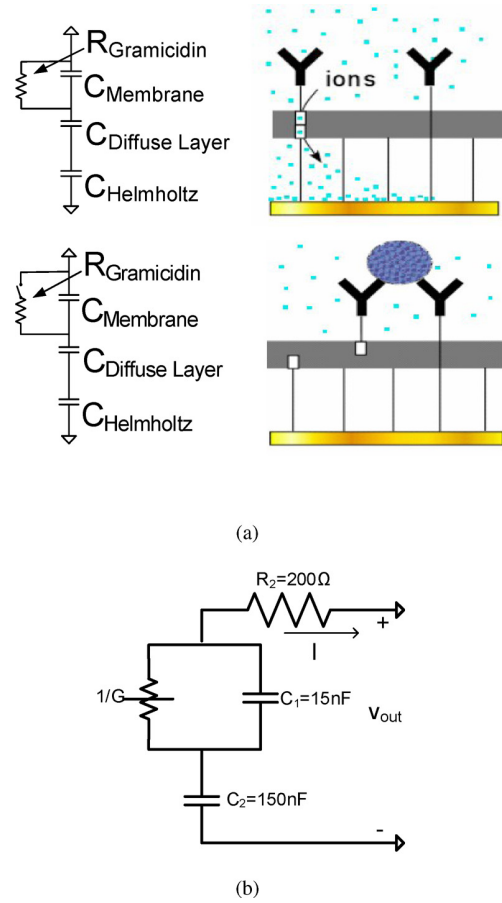


Fig. 1. ICS biosensor comprises an ion channel switch. (a) (Top) Switched-on state when the ion channels are conducting and (bottom) switched-off state when the ion channels are not conducting. The equivalent electrical circuit shown in Fig. 1(b) results in a second-order transfer function.

TABLE I
 TYPICAL VALUES FOR THE COMPONENTS OF THE EQUIVALENT ELECTRICAL SYSTEM OF THE ICS BIOSENSOR, DEPICTED IN FIG. 1(b)

Element	Value
Membrane Capacitance C_1	$0.5\mu\text{F}/\text{cm}^2$
Interfacial Capacitance C_2	$3.5\mu\text{F}/\text{cm}^2$
Biosensor Resistance $R_1 = 1/G$	$60\text{k}\Omega\text{--}600\text{k}\Omega$
Electrolyte Resistance R_2	200Ω

The area of the electrode is 0.03 cm^2 .

141 $I(s)$ denoting the Laplace transforms, the admittance transfer
 142 function of the equivalent circuit parameterized by G is

$$H(s) = \frac{I(s)}{V_{\text{out}}(s)} = \frac{s^2 + s a G}{s^2 R_2 + s(b_2 + b_1 G) + b_3 G}. \quad (1)$$

143 The constants in $H(s)$ are $a = 1/C_1$, $b_1 = R_2/C_1$, $b_2 =$
 144 $1/C_1 + 1/C_2$, and $b_3 = 1/C_1 C_2$.

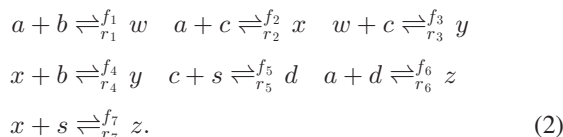
145 Electrodes in the 2009 generation ICS biosensors have an area
 146 of 0.03 cm^2 . The resistance of the biosensor when no analyte
 147 is present is approximately $60\text{ k}\Omega$. This can be reconciled with
 148 the $10^{11}\ \Omega$ per channel resistance of gramicidin A as follows.
 149 Since there are 10^8 gramicidin channels per centimeter square,
 150 each electrode of area 0.03 cm^2 contains approximately 3×10^6
 151 channels with approximately half of them dimerized. So, the

152 effective resistance of all the dimerized ion channels (which
153 act as parallel resistors) is approximately 60 k Ω . The measured
154 current is the average effect of the formation and disassociation
155 of thousands of dimers, and is approximately continuous valued.

156 B. Chemical Kinetics of the Biosensor

157 This section formulates the dynamics of the chemical reac-
158 tions in the biosensor with the goal of modeling how the biosen-
159 sor conductance G in (1) evolves. Recall that G decreases with
160 time if analyte molecules are present due to chemical reactions
161 that inhibit the formation of gramicidin dimers.

162 The reactions involved in the ICS biosensor stem from the
163 binding of analyte molecules to the binding sites on the mem-
164 brane followed by cross linking of the mobile ion channels to
165 these bound analytes. The species involved in these reactions
166 are separated into primary species and complexes. The pri-
167 mary species are analyte a with concentration A , binding sites
168 b with concentration B , free moving monomeric ion channels c
169 with concentration C , and tethered monomeric ion channels s
170 with concentration S . The complexes denoted as d , w , x , y , and
171 z with concentrations, D , W , X , Y , and Z are formed according
172 to the following chemical reactions:



173 In (2), f_i and r_i , for $i = \{1, 2, 3, 4, 5, 6, 7\}$, respectively, de-
174 note the *forward* and *backward* reaction rate constants. For
175 reactions occurring in 3-D space, such as binding of ana-
176 lyte with binding sites, the forward reaction rate constants
177 f_i have units of $\text{M}^{-1} \cdot \text{s}^{-1}$ (M denotes molar concentration,
178 i.e., moles per liter). For reactions occurring in 2-D space,
179 such as dimerization of the ion channel, f_i , have units of
180 centimeter square-per second per molecule. The backward re-
181 action rate constants r_i have units of per seconds.

182 The chemical reactions in (2) give a complete symbolic de-
183 scription of the operation of the ICS biosensor that was qual-
184 itatively described in Section II of the companion paper. The
185 forward part of the first equation reports on an analyte molecule
186 a being captured by a binding site b and the resulting complex
187 is denoted by w . The third equation states that a free moving
188 gramicidin monomer c in the outer leaflet of the bilayer lipid
189 membrane (BLM) can bind to the complex w , thus producing
190 another complex, denoted by y . An analyte molecule can also
191 be captured by the binding site linked to the freely diffusing
192 monomer c . The second equation states that this results in the
193 production of the complex x . The complex x can still diffuse
194 on the outer leaflet of the BLM, and hence can move toward a
195 tethered binding site b and bind to it, resulting in the complex y
196 (fourth equation). On the other hand, the complex x can diffuse
197 on top of the tethered ion channel monomer s , which results
198 in the production of complex z (seventh equation). The event
199 that determines the biosensor conductance (and thus the current
200 flowing through the biosensor) is the binding of the free moving
201 ion channel monomer c and the tethered ion channel monomer

TABLE II
CONCENTRATIONS OF PRIMARY SPECIES IN THE ICS BIOSENSOR

Initial Concentration of Species	Value
Mobile gramicidin A monomers $C(0)$	10^8 molecules/cm ²
Tethered gramicidin A monomers $S(0)$	10^9 molecules/cm ²
Dimer $D(0)$	10^8 molecules/cm ²
Tethered Binding Site $B(0)$	10^9 – 10^{11} molecules/cm ²
Analyte A^*	μM – fM

Recall 1 M (molar) concentration is 1 mol/L.

202 s . This results in the formation of a dimer d (fifth equation).
203 Indeed, the biosensor conductance is proportional to the dimer
204 concentration, i.e., $G(t) = \text{constant} \times D(t)$. Finally, an analyte
205 molecule can also bind to an already formed dimer, which again
206 produces the complex z (sixth equation).

207 We are now ready to formulate the chemical kinetics of the
208 ICS biosensor. The total reaction rates are straightforwardly
209 obtained from (2) as

$$\begin{aligned} R_1 &= f_1 AB - r_1 W & R_2 &= f_2 AC - r_2 X \\ R_3 &= f_3 WC - r_3 Y & R_4 &= f_4 XB - r_4 Y \\ R_5 &= f_5 CS - r_5 D & R_6 &= f_6 AD - r_6 Z \\ R_7 &= f_7 XS - r_7 Z. \end{aligned} \quad (3)$$

210 Define $u = \{B, C, D, S, W, X, Y, Z\}^T$ and $r(u(t)) = \{R_1,$
211 $R_2, R_3, R_4, R_5, R_6, R_7\}^T$, where T denotes transpose and R_i
212 are defined in (3). Then the nonlinear ordinary differential equa-
213 tion describing the dynamics of the chemical species is

$$\frac{d}{dt}u = Mr(u(t)) \quad (4)$$

$$\text{where } M = \begin{pmatrix} -1 & 0 & 0 & -1 & 0 & 0 & 0 \\ 0 & -1 & -1 & 0 & -1 & 0 & 0 \\ 0 & 0 & 0 & 0 & 1 & -1 & 0 \\ 0 & 0 & 0 & 0 & -1 & 0 & -1 \\ 1 & 0 & -1 & 0 & 0 & 0 & 0 \\ 0 & 1 & 0 & -1 & 0 & 0 & -1 \\ 0 & 0 & 1 & 1 & 0 & 0 & 0 \\ 0 & 0 & 0 & 0 & 0 & 1 & 1 \end{pmatrix}.$$

214 The initial concentrations of the primary species in $u(0)$, namely,
215 A^* , $B(0)$, $C(0)$, $S(0)$, and $D(0)$, are given in Table II. The initial
216 concentrations of the secondary species are zero. Note that in
217 Table II, $S(0)$ denotes the initial concentration of the tethered
218 gramicidin monomers. Also, $S \approx S(0)$ during the experiment.

219 The previous system of equations is obtained as follows. Con-
220 sider, for example, the primary species b in (2). According to
221 the first and fourth equations in (2), b is consumed when it
222 binds to a and x , and is produced when w and y decompose.
223 So the change in the concentration of b can be expressed as
224 $dB/dt = -R_1 - R_4$. This yields the first equation in the sys-
225 tem (4). The evolution of other species is derived similarly,
226 yielding (4).

227 Equation (4) is a complete representation of the chemi-
228 cal kinetics of the biosensor. Recall the biosensor conduc-
229 tance $G(t) = \text{constant} \times D(t)$, when $D(t)$ denotes the dimer

TABLE III
TYPICAL VALUES OF THE REACTION RATES f_i AND r_i FOR ANTIGEN-ANTIBODY PAIR hCG-IgG AND STREPTAVIDIN-BIOTIN PAIR

Reaction Rate	Streptavidin-Biotin	hCG-IgG
$f_1 = f_2 = f_6$	$7 \times 10^6 \text{ (M}^{-1}\text{s}^{-1}\text{)}$	$5 \times 10^5 \text{ (M}^{-1}\text{s}^{-1}\text{)}$
$f_3 = f_4$	$10^{-10} \text{ (cm}^2\text{s}^{-1}\text{molecule}^{-1}\text{)}$	$5 \times 10^{-11} \text{ (cm}^2\text{s}^{-1}\text{molecule}^{-1}\text{)}$
$f_5 = f_7$	$10^{-11} \text{ (cm}^2\text{s}^{-1}\text{molecule}^{-1}\text{)}$	$10^{-11} \text{ (cm}^2\text{s}^{-1}\text{molecule}^{-1}\text{)}$
$r_1 = r_2 = r_6$	$10^{-6} \text{ (s}^{-1}\text{)}$	$10^{-4} \text{ (s}^{-1}\text{)}$
$r_3 = r_4$	$10^{-6} \text{ (s}^{-1}\text{)}$	$10^{-4} \text{ (s}^{-1}\text{)}$
$r_5 = r_7$	$10^{-2} \text{ (s}^{-1}\text{)}$	$10^{-2} \text{ (s}^{-1}\text{)}$

hCG is human chorionic gonadotropin and IgG is immunoglobulin G. The concentration of the glycoprotein hormone in a woman's blood or urine, increase by to 10^5 during the early stages of pregnancy.

concentration as a function of time and is obtained by solving (4). However, note that (4) does not model the dynamics of the analyte concentration A . The dynamics of $A(x_1, x_2, x_3, t)$ over space (x_1, x_2, x_3) and time t are given by the mass transport partial differential equation, see Section III-B.

Example: Table III gives the typical forward and backward reaction rate constants (f_i, r_i) for two important examples. The first example deals with protein-receptor interaction such as the detection of the protein streptavidin by using biotin as the binding site. The second example in Table III deals with antigen-antibody interaction such as the detection of the pregnancy hormone [human chorionic gonadotropin (hCG)] by using the antibody immunoglobulin G (IgG) as the binding sites of the biosensor. We will use these values in Section III-A when identifying the fast and slow dynamics of (4).

C. Black-Box Model for Biosensor Response to Analyte

The final step in this modeling section is to describe the input/output behavior of the biosensor. This can be viewed as a "black-box model" in comparison to the previous two sections where physical/chemical laws were used to construct a "white-box" model. Let $n = 0, 1, \dots$ denote discrete time (with typical sampling interval of 1 s) and A denote the concentration of analyte. As described earlier, the presence of analyte results in a decrease of the biosensor conductance G in (1). Detailed experimental analysis of the biosensor response show that G evolves in discrete time according to one of the three different concentration modes \mathcal{M} :

$$G_{n+1} = f^{\mathcal{M}}(G_n, A) + w_n$$

$$\mathcal{M} = \begin{cases} 1, & A \text{ is low: } f^1(G_n, A) = G_n + \kappa_0 \\ 2, & A \text{ is medium: } f^2(G_n, A) = \kappa_1 G_n + \kappa_2 \\ 3, & A \text{ is high: } f^3(G_n, A) = \kappa_3 G_n + \kappa_4 \end{cases} \quad (5)$$

where $\kappa_0, \kappa_1, \kappa_2, \kappa_3,$ and κ_4 are constants, with $|\kappa_1|, |\kappa_3| < 1$ to ensure stability of the system (5). The variable w_n is a noise process that models our uncertainty in the evolution of G . The function $f^{\mathcal{M}}$ models the fact that the biosensor conductance G_n decreases according to one of the three distinct modes depending on the analyte concentration A . For low (or no) analyte present ($\mathcal{M} = 1$), the conductance decreases linearly. For medium and high concentrations ($\mathcal{M} = 2, \mathcal{M} = 3$), the decrease in conductance is exponential with different decay rates. High analyte concentration refers to ($A \geq 10^{-8}$ M) and medium analyte concentration refers to ($A \geq 10^{-9}$ M). In Section III-A, we show

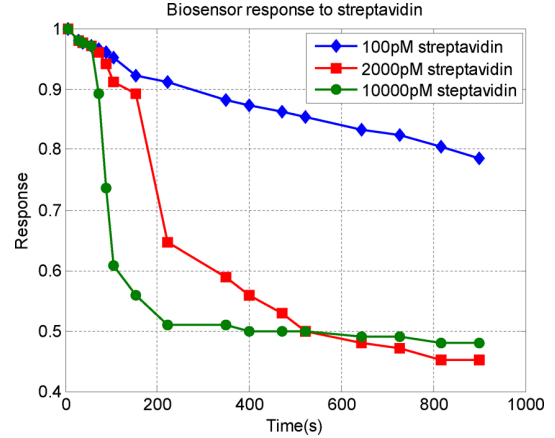


Fig. 2. Biosensor response to streptavidin. The figure demonstrates two modes of decay of the response of the system conductance G [Ω^{-1}] depending on the analyte concentration, namely, linear and exponential; see [17] and [18] for details.

that these three distinct modes of behavior, observed in the experimental analysis of the biosensor, can be obtained via singular perturbation analysis of the chemical kinetics of the biosensor.

Fig. 2 shows examples of the biosensor response to streptavidin with different concentrations and provides a clear demonstration of the different kinetic regimes of the sensor function; see [17] and [18] for details. The streptavidin-biotin binding pair is one of the strongest and best characterized interactions available, and is used as a model system in this paper.

III. ANALYTE FLOW AND BIOSENSOR DYNAMICS

Having formulated models for the electrical response and chemical kinetics, we are now ready to analyze these models to predict the ICS biosensor's response. We will determine how the chemical kinetics (4) interact with the partial differential equation of mass transport of analyte $A(x_1, x_2, x_3, t)$. Here, $x_1, x_2,$ and $x_3,$ respectively, denote the $x, y,$ and z spatial axes, and t denotes continuous time. Substantial insight is gained by considering the following two important subcases.

Case 1 (Reaction-rate-limited kinetics): In the reaction-rate-limited kinetics regime, large analyte flow rates, high analyte concentration, or low binding site densities (e.g., milliliter per minute flow rate, micromolar concentration, or less than 10^8 binding sites per centimeter square) compensate for the depletion of analyte molecules due to rapid reaction at the biomimetic

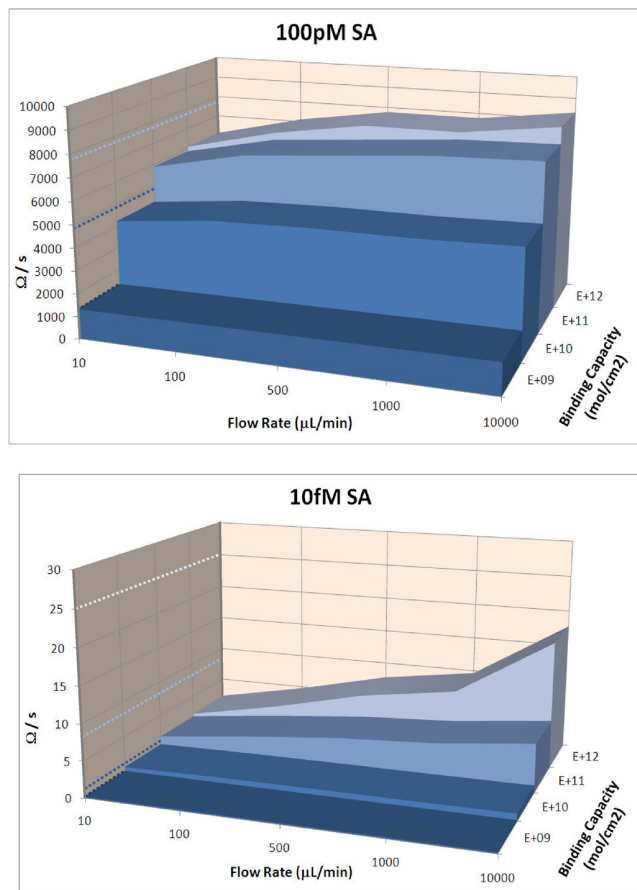


Fig. 3. Biosensor response to 100 pM and 10 fM concentrations of streptavidin for various binding site to ion channel densities and flow rates. At 100 pM and low binding site densities, increasing flow rate (left to right) has little effect. At 10 fM and high binding site densities, flow rate has a large effect. High flow limits are shown as dashed lines on the left.

analyte concentration and high binding site density, a high flow rate is required to achieve a measurable response. This corresponds to mass-transport-influenced kinetics (case 2), [19]. It is also apparent from Fig. 3 that a high binding site density is essential for high sensitivity. With high binding site density, target molecules collide more frequently with receptors, and are thus captured more quickly. The greater the ratio of binding site density to analyte concentration, the faster the response of the biosensor.

A. Case 1: Reaction-Rate-Limited Kinetics

In this section, the chemical kinetics in the reaction-rate-limited regime (constant analyte concentration $A^* > 1 \mu\text{M}$) are analyzed as a two-timescale dynamical system. We will use singular perturbation theory to approximate the time evolution of dimer concentration.

To determine the slow and fast modes of the nonlinear chemical kinetics depicted in (3) and (4), we compute the eigenvalues λ_i of the linearized version of (4). For typical parameter values of the ICS biosensor in Tables II and III, $|\lambda_{7,8}| \gg |\lambda_{1,2,3,4,5,6}|$. Therefore, species Y and Z decay at a rate much faster than the other species. Accordingly define the fast species $\beta = \{Y, Z\}$ and slow species $\alpha = \{B, C, D, S, W, X\}$. Let $g(\alpha, \beta)$ denote the vector field of the fast variables and $f(\alpha, \beta)$ the vector field of the slow variables. Equations (3) and (4) can now be expressed as a two-timescale system [initial conditions $\alpha(0)$ and $\beta(0)$ are specified next (4)]

$$\frac{d\alpha}{dt} = f(\alpha, \beta) \quad \epsilon \frac{d\beta}{dt} = g(\alpha, \beta) \quad (6)$$

where $\epsilon \approx 1/|\lambda_7| = 10^{-2}$ is chosen as the smallest time constant of the governing differential equations [2].

The following theorem uses basic singular perturbation theory, specifically Tikhonov's theorem, [2, Sec. 11.1], as well as the approximate relation $S \approx S(0)$ to simplify the aforementioned two-timescale nonlinear system. The resulting simplified system yields the evolution of biosensor conductance versus analyte concentration according to the modes described in Section II-C, namely, linear and exponential decays.

Theorem 3.1: Consider the chemical species dynamics depicted by the two-timescale system (6). Then, as $\epsilon \rightarrow 0$, the dimer concentration $D(t)$ converges to the trajectory $\bar{D}(t)$ defined by the following system:

$$\frac{d}{dt} \bar{D} = -\bar{D}(r_5 + f_6 A^*) + \left(f_5 C + \frac{r_6 f_7 X}{r_6 + r_7} \right) S(0). \quad (7)$$

More specifically, suppose the initial dimer concentration $D(0)$ at time $t = 0$ is within an $O(\epsilon)$ neighborhood of $\beta = h(\alpha)$, where $h(\alpha)$ denotes the solution of the algebraic equation $g(\alpha, \beta) = 0$ in (6). Then, for all time $t \in [0, T]$, $|D(t) - \bar{D}(t)| = O(\epsilon)$, where $T > 0$ denotes a finite time horizon.

Theorem 3.1 exploits the two-timescale nature of the chemical kinetics (6) to arrive at an approximate equation (7) for the dimer concentration $D(t)$, which is within $O(\epsilon)$ of the true solution. The proof follows from verifying the conditions of Theorem 11.1 in [2, Sec.11.1], and is omitted due to lack of

surface populated by the binding sites. In this regime, it is reasonable to assume that the analyte concentration is approximately constant over space and time, i.e., $A(x_1, x_2, x_3, t) = A^*$, where A^* denotes a constant analyte concentration. We consider this case in Section III-A, where we will mathematically justify the black-box model (5) by applying singular perturbation analysis to the white-box model developed earlier. We will derive the empirically observed black-box model (5).

Case 2 (Mass-transport-influenced kinetics): Here, the biosensor chemical kinetics are influenced by both mass transport and reaction rates. Therefore, the local concentration of analyte $A(x_1, x_2, x_3, t)$ varies over space and time. In Section III-B, we model the change in analyte concentration over time and space by a boundary value partial differential equation.

Why do analyte mass transport kinetics matter? We start with the following motivating example. Fig. 3 shows quantitative predictions of the change in the biosensor resistance per unit time for various binding site densities and sample flow rates for high analyte concentrations (100 pM) and low analyte concentrations (10 fM). As shown in Fig. 3, at high analyte concentrations, the biosensor response is insensitive to flow rate. This corresponds to the reaction-rate-limited kinetics (case 1). However, for low

space. However, here is some intuition. It can be shown that as $\epsilon \downarrow 0$, the fast dynamics approach the quasi steady state $h(\alpha)$ defined in the theorem. This quasi steady state $h(\alpha)$ of the fast variables β is then substituted in the slow dynamics in (6), which results in the following approximate dynamics for the slow species: $d\bar{\alpha}/dt = f(\bar{\alpha}, h(\bar{\alpha}))$. We are interested in a specific component of $\bar{\alpha}$, namely, the approximate dimer concentration \bar{D} , which can be shown to evolve according to (7).

We can now analyze the response of the biosensor to different analyte concentrations A^* . Discretizing (7) using Euler's method with step size $h > 0$ yields

$$D_{n+1} = (1 - (r_5 + f_6 A^*)h) D_n + h \left(S(0) \left(\frac{f_5 C(r_6 + r_7) + r_6 f_7 X}{r_6 + r_7} \right) \right). \quad (8)$$

Therefore, the dimerconcentration of the biosensor D evolves according to one of the following three modes, depending on the concentration of the analyte A^* :

$$D_{n+1} = f^{\mathcal{M}}(D_n, A^*) + w_n$$

$$\mathcal{M} = \begin{cases} 1, & A^* \text{ is low: } f^1(D_n, A^*) = D_n + \kappa_0 \\ 2, & A^* \text{ medium: } f^2(D_n, A^*) = \kappa_1 D_n + \kappa_2 \\ 3, & A^* \text{ high: } f^3(D_n, A^*) = \kappa_3 D_n + \kappa_4 \end{cases} \quad (9)$$

where the noise w_n is defined similarly to (5). The constants κ_i for $i \in \{1, 2, 3, 4\}$ are computed as

$$\kappa_1 = \kappa_3 = (1 - (r_5 + f_6 A^*)h)$$

$$\kappa_2 = \kappa_4 = h \left(S(0) \left(\frac{f_5 C(r_6 + r_7) + r_6 f_7 X}{r_6 + r_7} \right) \right). \quad (10)$$

Summary: We have shown that the dimer concentration evolves according to three distinct modes that depend on the analyte concentration. Using (9), since the conductance G is directly proportional to dimerconcentration D , we arrive at the black-box model (5) of Section II-C, which was based on experimental observations.

B. Case 2: Mass Transport Kinetics

Here, we consider the second subcase where the ratio of analyte concentration to binding site density is small [e.g., $A/B = 1 \text{ pM}/10^9 = 10^{-21}$, see (2)]. Then mass transport effects become the dominant criterion in achieving an acceptable response rate of the biosensor to analyte. The analyte concentration is no longer a constant A^* , but a function of time and space $A(x_1, x_2, x_3, t)$. In this section, the partial differential equation governing the mass transport of analyte molecules is derived.

Analyte is transported to the reacting surface of the ICS biosensor, by diffusion and flow, where it reacts with the immobilized receptors. The flow chamber used for the biosensor has a rectangular cross section, and is illustrated in Fig. 4, where the height of the chamber along the x_3 -axis is $h = 0.1 \text{ mm}$. The length of the chamber along the x_1 -axis is $L = 6 \text{ mm}$ and the width of the chamber along the x_2 -axis is $W = 2 \text{ mm}$.

It is shown in [20] that when the aspect ratio h/W is small (e.g., less than 0.1), the variations in analyte concentration along

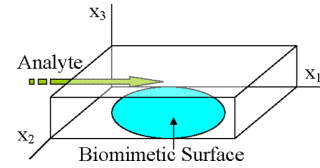


Fig. 4. Schematic of the flow chamber. The reactive surface is located at $x_3 = 0$. The solution containing the analyte enters at $x_1 = 0$ and flows along the x_1 -axis.

the width of a flow chamber are negligible. In the case of ICS biosensor with flow chamber shown in Fig. 4, the aspect ratio is 0.05. So we can ignore the variations along the x_2 -axis and the analyte concentration is $A(x_1, x_3, t)$. In the flow chamber, the analyte concentration $A(x_1, x_3, t)$ is governed by the following reaction-diffusion partial differential equation [5]

$$\frac{\partial A}{\partial t} = \gamma \left(\frac{\partial^2 A}{\partial x_1^2} + \frac{\partial^2 A}{\partial x_3^2} \right) - v \frac{\partial A}{\partial x_1} \quad (11)$$

where γ is the diffusivity constant of the analyte (e.g., $\gamma \approx 10^{-6} \text{ cm}^2 \cdot \text{s}^{-1}$ for streptavidin or hCG) and v denotes the flow rate of the sample containing the analyte. There are four boundary conditions that need to be considered.

- 1) The chamber boundary at $x_3 = h$ is reflective and the mass flux must equal zero. This yields the Neumann boundary condition

$$\left. \frac{\partial A}{\partial x_3} \right|_{(x_1, x_3=h, t)} = 0. \quad (12)$$

- 2) At the biomimetic surface, $x_3 = 0$, the mass flux must equal the time rate of change of the concentration of the species that combine with a . This results in the Neumann boundary condition

$$\left. \frac{\partial A}{\partial x_3} \right|_{(x_1, x_3=0, t)} = -\frac{1}{\gamma} \left(\frac{\partial X}{\partial t} + \frac{\partial W}{\partial t} + \frac{\partial Z}{\partial t} \right). \quad (13)$$

The chemical kinetics $\partial X/\partial t$ and $\partial W/\partial t$ are defined in (4).

- 3) At the entry to the flow cell, $x_1 = 0$, the analyte concentration is equal to the injection concentration \bar{A} , and at $x_1 = L$, where the analyte exits, the mass flux is zero. These yield the third (Dirichlet) and fourth (Neumann) boundary conditions

$$A(x_1 = 0, x_3, t) = \bar{A} \quad \left. \frac{\partial A}{\partial x_1} \right|_{(x_1=L, x_3, t)} = 0. \quad (14)$$

Summary: The analyte concentration $A(x_1, x_3, t)$ is obtained by solving (11) subject to mixed Neumann and Dirichlet boundary conditions (12)–(14).

C. Model Evaluation

How good are the aforementioned models in predicting the ICS biosensor response? We conducted experiments on the ICS biosensor for detecting streptavidin at concentrations of 10 and 100 fM, and 10 pM. Fig. 5 illustrates the highly sensitive response of the biosensor and how this response depends on the

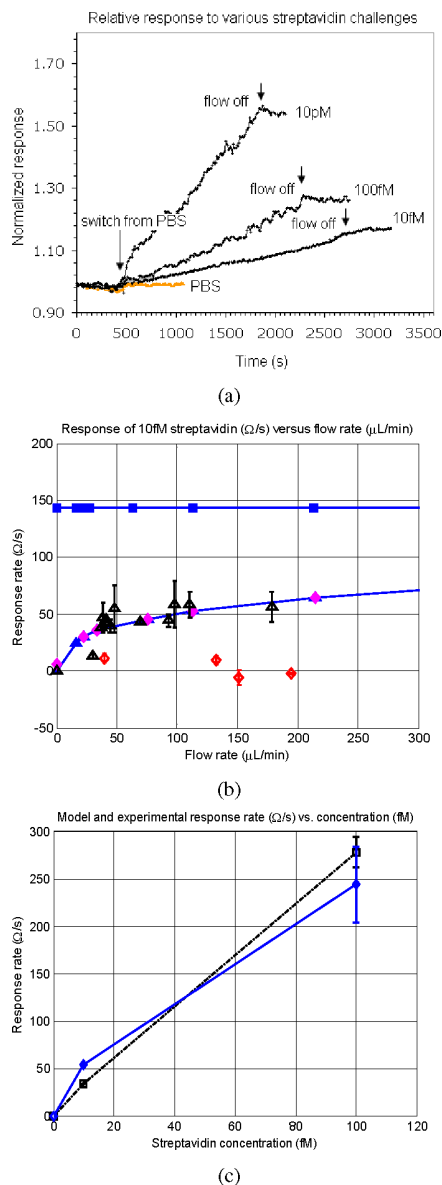


Fig. 5. (a) Response of ICS sensor for the concentrations shown and $150 \mu L/min$ flow rate. When the flow stops (indicated by arrows in the figure), the response stops at all concentrations. This is due to analyte depletion at the sensor surface. (b) Dependency of response of sensor to flow rate (black dots). The lines (purple) through the data points are predicted by the model. The straight line at $150 \Omega/s$ is the high flow response limit. The red diamonds are phosphate buffer saline (PBS) controls. (c) Predicted and experimental titration curves for the ICS sensor response to streptavidin in the range $1-100 \text{ fM}$ at $150 \mu L/min$. The triangles are experimental data and the diamonds are from the model.

“purge time” required at this flow rate for the bolus to purge the residual buffer from the line. Our experiments show that at this “purge time,” the resistance started to increase. When the flow was stopped, the resistance increase stopped, as depicted by the arrows in Fig. 5(a). Restarting the flow caused the resistance rise to recommence.

The aforementioned experimentally measured response rate of the biosensor was compared with that predicted by our model. We computed the predicted response as follows. The mass transport effects were computed by solving (11) subject to boundary conditions (12)–(14) via the finite-element method on the rectangular flow cell shown in Fig. 4. The chemical kinetics were computed by solving (4) numerically. This yields the dimer concentration $D(t)$ in (4) and also the biosensor conductance G . Fig. 5(b) shows the experimentally measured response rate (black dots) to 10 fM streptavidin at various flow rates from 0 to $200 \mu L/min$. Also shown (in purple) is the theoretical response rate predicted by our model. As can be seen by eyeballing the plots, the predicted performance of the biosensor closely matches the experimental performance. Fig. 5(b) shows the experimental and predicted response rate in the reaction-rate-limited region of operation. Finally, Fig. 5(c) shows the predicted and experimental response rate in the range of $0-100 \text{ fM}$ streptavidin. It confirms that the biosensor response rate increases with analyte concentration.

IV. SIGNAL PROCESSING WITH BIOSENSOR

Our goal in this section is to describe how the measurements from the biosensor can be used to detect the presence and concentration of analytes. Today’s generation of ICS biosensor has electrodes of 1 mm radius comprising millions of individual gramicidin channels. The measured current is of the order of microamperes. The measurement noise is insignificant (apart from a slow baseline drift). So, for the ICS biosensor, the concentration of the analyte can be determined straightforwardly from the three dynamic modes described in (5). It is a future goal to miniaturize these electrodes. Electrode sizes of $1 \mu m$ radius comprise only a few ion channels. The current pulses from individual channels can be resolved and the biosensor records a finite-state “digital” output. The arrival of individual analyte molecules can then be detected at individual electrodes. This allows for exploitation of the analyte flow equations in Section III-B for measurements at multiple electrodes resulting in enhanced sensitivity. The noise levels are substantial and careful modeling of the noise distribution is required.

Construction of ICS biosensors with microelectrodes is the subject of our on-going research. Here, we provide a proof of concept of the signal processing capabilities by using a simpler biosensor setup, see [21] for experimental details. For experimental convenience, we used a covalently linked dimer of gramicidin ion channels (called bisgramicidin A) incorporated into an untethered bilayer membrane excised from a giant lipid vesicle seen in Fig. 6. The bilayer is supported over the $1 \mu m$ diameter opening of a micropipette as shown in Fig. 7.

With the biosensor setup shown in Fig. 7, the contact area between the micropipette and liposome contains only $2-5$ bis-

analyte flow rate. Fig. 5(a) shows the experimentally observed increase in biosensor resistance for flow rate $v = 150 \mu L/min$. It shows that as the analyte concentration is increased, the biosensor exhibits faster response. It is remarkable that the biosensor responds to concentrations as low as 10 fM . To validate this experimental response, several tests were conducted in which a bolus of streptavidin at 10 fM , 100 fM , or 10 pM was added to the feed line, requiring 20 min to reach the sensor. The line was operated at a constant flow rate of $150 \mu L/min$. We computed the

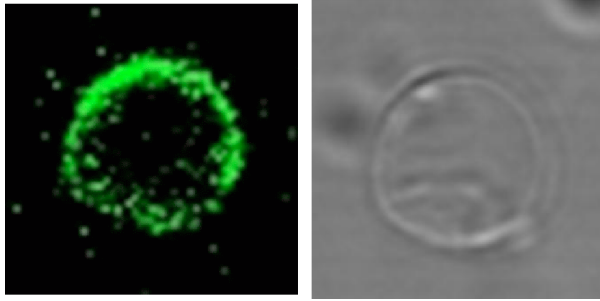


Fig. 6. (Left) Fluorescence image of biosensor's horizontal optical section shows the bisgramicidin A channels labeled using fluorescein isothiocyanate (FITC) and identified by the green color. (Right) Phase-contrast image of the same horizontal slice shows the overall shape of the biosensor.

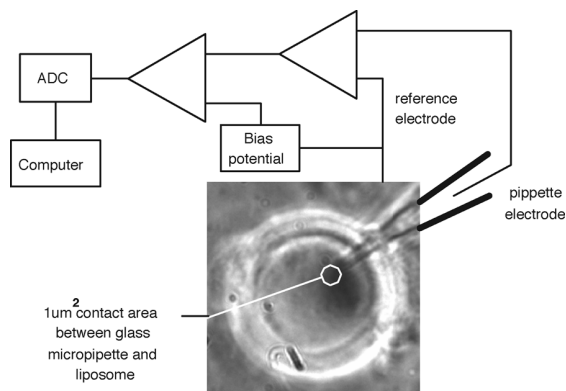


Fig. 7. Photograph of glass micropipette and liposome, with block diagram of the electrical detection scheme. The solution in the recording pipette was 0.5 M KCl with the liposomes suspended in a 0.5-M NaCl solution. The conductance of bisgramicidin channels under these conditions is approximately 20 pS.

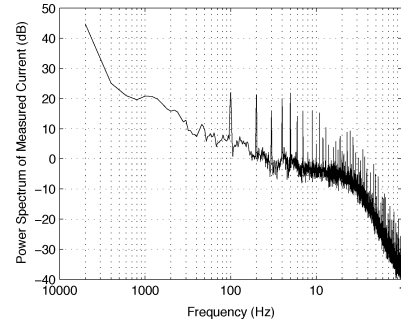


Fig. 8. Power spectral density of biosensor response clearly shows the $1/f$ open channel noise and the antialiasing effect.

refer to [21] for details of the HMM classifier equations and performance of the biosensor on experimental data.

V. CONCLUSIONS AND EXTENSIONS

In this paper, we constructed models for the electrical, chemical, and analyte mass transport dynamics of the ICS biosensor. The chemical kinetics of the biosensor were modeled as a two-timescale nonlinear dynamical system in the reaction-rate-limited case. Using singular perturbation theory, we explained mathematically the experimentally observed behavior of the biosensor to analyte concentration. For low analyte concentrations, mass transport dynamics became the dominant design constraint. By comparing with the experimental response, we showed that the mass transport flow model coupled with chemical kinetics accurately predict the biosensor response. Finally, for micro-sized electrodes, we described how statistical signal processing algorithms can be used to classify the analyte concentration.

When employing antibodies or other well-defined receptors, stochastic detection in conjunction with spatial analysis across an electrode array can yield improved sensitivity in the biosensor. An extension of this study is to examine the coherence of channel noise across such an array of electrodes. We anticipate an improvement in detection threshold proportional to N rather than \sqrt{N} , where N is the number of independently read electrodes in the array. Such enhanced versions of the biosensor will yield performance closer to the capabilities of antennae in moths and the olfaction receptor epithelia in dogs.

REFERENCES

- [1] B. Cornell, V. L. Braach-Maksvytis, L. G. King, P. D. Osman, B. Raguse, L. Wiecezorek, and R. J. Pace, "A biosensor that uses ion-channel switches," *Nature*, vol. 387, pp. 580–583, 1997.
- [2] H. K. Khalil, *Nonlinear Systems*, 3rd ed. Englewood Cliffs, NJ: Prentice-Hall, 2002.
- [3] G. Q. Dong, L. Jakobowski, M. A. J. Iafolia, and D. R. McMillen, "Simplification of stochastic chemical reaction models with fast and slow dynamics," *J. Biol. Phys.*, vol. 33, no. 1, pp. 67–95, Feb. 2007.
- [4] T. Mason, A. R. Pineda, C. Wofsy, and B. Goldstein, "Effective rate models for the analysis of transport-dependent biosensor data," *Math. Biosci.*, vol. 159, pp. 123–144, 1999.
- [5] D. A. Edwards, "Estimating rate constants in a convection-diffusion system with a boundary reaction," *IMA J. Appl. Math.*, vol. 63, pp. 89–112, 1999.
- [6] B. Goldstein, D. Coombs, X. He, A. R. Pineda, and C. Wofsy, "The influence of transport on the kinetics of binding to surface receptors:

gramicidin channels. So the measured current is of the order of tens of picoamperes and measurement noise becomes a significant issue. The combined response of these channels yields a finite-state signal that can be modeled as a finite-state Markov chain (see [21] for details). The current pulses that generate this finite-state signal are thought to arise from conformational interconversion in the bisgramicidin A secondary structure [22]. The measured biosensor signal can be modeled as a noisy finite-state Markov chain, i.e., a hidden Markov model (HMM) [15]. Modeling the noise is a challenging task. It arises from thermal noise, the antialiasing effect from sampling, and an open channel noise with its power proportional to the inverse of frequency. Fig. 8 shows the power spectral density of a typical sequence of biosensor recordings, and shows that the power decreases at a rate of -10 dB/dec at low frequencies, indicating the presence of $1/f$ noise. This $1/f$ noise is discussed in other studies of bisgramicidin A ion channels, see [23]. To model this correlated noise process, we used an autoregressive (AR) Gaussian process that comprises white Gaussian noise process W_k filtered by an all-pole filter, see [21] for the use of Ljung-box test for model adequacy.

Having verified the adequacy of the HMM for representing the biosensor current, it is straightforward to construct an HMM maximum-likelihood classifier to detect analyte molecules. We

- 568 Application to cell and BIAcore,” *J. Mol. Recognit.*, vol. 12, pp. 293–
569 299, 1999.
- 570 [7] B. Hille, *Ionic Channels of Excitable Membranes*, 3rd ed. Sunderland,
571 MA: Sinauer Associates, Inc., 2001.
- 572 [8] K. Cole, *A Quantitative Description of Membrane Current and Its Appli-*
573 *cation to Conductance and Excitation in Nerve*. Berkeley, CA: Univ. of
574 California Press, 1968.
- 575 [9] D. Lauffenburger and J. K. Linderman, *Receptors—Models for Binding,*
576 *Trafficking and Signaling*. New York, Oxford, 1993.
- 577 [10] S. Qian and H. H. Bau, “A mathematical model of lateral flow bioreactions
578 applied to sandwich assays,” *Anal. Biochem.*, vol. 322, pp. 89–98, 2003.
- 579 [11] H. J. Kushner, *Weak Convergence and Singularly Perturbed Stochastic*
580 *Control and Filtering Problems*. Boston, MA: Birkhauser, 1990.
- 581 [12] R. W. Glaser, “Antigen-antibody binding and mass transport by convection
582 and diffusion to a surface: A two-dimensional computer model of binding
583 and dissociation kinetics,” *Anal. Biochem.*, vol. 213, pp. 152–161, 1993.
- 584 [13] D. G. Myszka, T. A. Morton, M. L. Doyle, and I. M. Chaiken, “Kinetic
585 analysis of a protein antigen-antibody interaction limited by mass transport
586 on an optical biosensor,” *Biophys. Chem.*, vol. 64, pp. 127–137, 1997.
- 587 [14] M. Dehghan, “Numerical solution of the three-dimensional advection-
588 diffusion equation,” *Appl. Math. Comput.*, vol. 150, pp. 5–19, 2004.
- 589 [15] Y. Ephraim and N. Merhav, “Hidden Markov processes,” *IEEE Trans.*
590 *Inf. Theory*, vol. 48, no. 6, pp. 1518–1569, Jun. 2002.
- 591 [16] S. H. Chung, O. Anderson, and V. Krishnamurthy, Eds., *Biological Mem-*
592 *brane Ion Channels: Dynamics, Structure and Applications*. New York:
593 Springer-Verlag, 2007.
- 594 [17] B. Cornell, “Membrane-based biosensors,” in *Optical Biosensors: Present*
595 *and Future*, F. S. Ligler and C. A. R. Taitt, Eds. Amsterdam, The
596 Netherlands: Elsevier, 2002, p. 457.
- 597 [18] G. Woodhouse, L. King, L. Wiczorek, P. Osman, and B. Cornell, “The ion
598 channel switch biosensor,” *J. Mol. Recognit.*, vol. 12, no. 5, pp. 328–334,
599 1999.
- 600 [19] R. A. Vijayendran, F. S. Ligler, and D. E. Leckband, “A computational
601 reaction-diffusion model for analysis of transport-limited kinetics,” *J.*
602 *Anal. Chem.*, vol. 71, pp. 5405–5412, 1999.
- 603 [20] J. P. Brody, P. Yager, R. E. Goldstein, and R. H. Austin, “Biotechnology
604 at low Reynolds numbers,” *Biophys. J.*, vol. 71, pp. 3430–3441, 1996.
- 605 [21] V. Krishnamurthy, K. Luk, B. Cornell, and D. Martin, “Gramicidin ion
606 channel based nano-biosensors: Construction, stochastic dynamical mod-
607 els and statistical detection algorithms,” *IEEE Sens. J.*, vol. 7, no. 9,
608 pp. 1281–1288, Sep. 2007.
- 609 [22] C. J. Stankovic, S. H. Heinemann, and S. L. Schreiber, “Immobilizing the
610 gate of a tartaric acid-gramicidin a hybrid channel molecule by rational
611 design,” *J. Amer. Chem. Soc.*, vol. 112, pp. 3702–3704, 1990.
- 612 [23] R. Sauve and G. Szabo, “Interpretation of $1/f$ fluctuations in ion conducting
613 membranes,” *J. Theor. Biol.*, vol. 113, pp. 501–516, Apr. 1985.



Sahar Moradi Monfared received the Bachelor’s
degree in electrical engineering in 2007 from the Uni-
versity of British Columbia, Vancouver, BC, Canada,
where she is currently working toward the Master’s
of Applied Science degree in electrical engineering.

637
638
639
640
641
642



Bruce Cornell was a Commonwealth Scientific and
Industrial Research Organization (CSIRO) Postdoc-
toral Fellow at the University of London during 1975–
1977. and He was a Senior Scientist with CSIRO
in the field of biophysics at Australia. He was ap-
pointed the Director of the Cooperative Research
Centre for Molecular Engineering during 1992–1999
and founded the commercial consortium that became
Ambri Ltd., for whom he worked as Chief Scientist
during 2000–2005. In 2005, he founded Surgical Di-
agnostics Ltd., St Leonards, N.S.W., Australia, where

643
644
645
646
647
648
649
650
651
652
653
654
655
656
657
658
659
660
661
662
663
664
665
666
667
668
669
670
671
672
673
674
675
676
677
678
679
680
681
682
683
684
685
686
687
688
689
690
691
692
693
694
695
696
697
698
699
700
701
702
703
704
705
706
707
708
709
710
711
712
713
714
715
716
717
718
719
720
721
722
723
724
725
726
727
728
729
730
731
732
733
734
735
736
737
738
739
740
741
742
743
744
745
746
747
748
749
750
751
752
753
754
755
756
757
758
759
760
761
762
763
764
765
766
767
768
769
770
771
772
773
774
775
776
777
778
779
780
781
782
783
784
785
786
787
788
789
790
791
792
793
794
795
796
797
798
799
800
801
802
803
804
805
806
807
808
809
810
811
812
813
814
815
816
817
818
819
820
821
822
823
824
825
826
827
828
829
830
831
832
833
834
835
836
837
838
839
840
841
842
843
844
845
846
847
848
849
850
851
852
853
854
855
856
857
858
859
860
861
862
863
864
865
866
867
868
869
870
871
872
873
874
875
876
877
878
879
880
881
882
883
884
885
886
887
888
889
890
891
892
893
894
895
896
897
898
899
900
901
902
903
904
905
906
907
908
909
910
911
912
913
914
915
916
917
918
919
920
921
922
923
924
925
926
927
928
929
930
931
932
933
934
935
936
937
938
939
940
941
942
943
944
945
946
947
948
949
950
951
952
953
954
955
956
957
958
959
960
961
962
963
964
965
966
967
968
969
970
971
972
973
974
975
976
977
978
979
980
981
982
983
984
985
986
987
988
989
990
991
992
993
994
995
996
997
998
999
1000

he is currently the Director of Science and Technology. He is an elected Mem-
ber of the Australian Academy of Technological Sciences and Engineering, and
a member of a number of advisory groups to Australian Universities and an
advisory to the Australian Government on the Medical Device Industry.

Q2
657
658

614
615
616
617
618
619
620
621
622
623
624



Vikram Krishnamurthy (S’90–M’91–SM’99–F’05)
was born in 1966. He received the Bachelor’s degree
from the University of Auckland, Auckland, New
Zealand, in 1988, and the Ph.D. degree from the
Australian National University, Canberra, A.C.T.,
Australia, in 1992.

He currently is a Professor and Canada Re-
search Chair in the Department of Electrical Engi-
neering, University of British Columbia, Vancouver,
BC, Canada. Prior to 2002, he was a Chaired Pro-
fessor in the Department of Electrical and Electronic

Engineering, University of Melbourne, Australia, where he was also the Deputy
Head. His current research interests include computational game theory and
stochastic control in sensor networks, and stochastic dynamical systems for
modeling of biological ion channels and biosensors.

Dr. Krishnamurthy has been the Editor-in-Chief of the IEEE JOURNAL SE-
LECTED TOPICS IN SIGNAL PROCESSING since 2010. He was Associate Editor
for several journals including the IEEE TRANSACTIONS AUTOMATIC CONTROL
the IEEE TRANSACTIONS ON SIGNAL PROCESSING the IEEE TRANSACTIONS
AEROSPACE AND ELECTRONIC SYSTEMS the IEEE TRANSACTIONS NANOBIO-
SCIENCE and the *Systems and Control Letters*. During 2009 and 2010, he was a
Distinguished Lecturer for the IEEE Signal Processing Society.

636